Article

A Lateral-Directional Control Method for High Aspect Ratio Full-Wing UAV and Flight Tests

Zhenyu Ma [1,2,*] **, Xiaoping Zhu** [2] **, Zhou Zhou** [2,3] **, Xu Zou** [3] **and Xin Zhao** [3]

[1] School of Astronautics, Northwestern Polytechnical University, Xi'an 710072, China
[2] UAV Research Institute, Northwestern Polytechnical University, Xi'an 710065, China;
    zhuxp@nwpu.edu.cn (X.Z.); zhouzhou@nwpu.edu.cn (Z.Z.)
[3] School of Aeronautics, Northwestern Polytechnical University, Xi'an 710072, China;
    zouxumail@mail.nwpu.edu.cn (X.Z.); xin_zhao@mail.nwpu.edu.cn (X.Z.)
* Correspondence: mazhenyu_nwpu@163.com

check for updates

Abstract: To solve the lateral-directional control problem of the high aspect ratio full-wing unmanned aerial vehicle (UAV) without an aileron and rudder, a control method is proposed that uses the differential thrust of propellers as the control output and the yaw angle as the controlled attitude angle. Meanwhile, simulation analysis and experimental verification are carried out. First, a lateral-direction mathematical model and a differential thrust of propeller model of the full-wing drone are established. The influence of the aerodynamic derivative $C_{Y\beta}$ on the lateral-direction mode is analyzed. Second, based on nonlinear dynamic inversion (NDI) and active disturbance rejection control (ADRC) theories, a yaw angle controller that uses the differential thrust of propellers as the control output is designed. Finally, the vector field (VF) method is improved to obtain the straight-line trajectory tracking method satisfying different speeds, and the logic of waypoint switching is given. The research shows that $C_{Y\beta}$ has a great influence on the dutch roll damping of the drone. For the full-wing configuration, it is feasible to use the yaw angle as the controlled attitude angle without considering the roll angle. The simulation and experimental results show that the designed lateral-directional control method for the high aspect ratio full-wing UAV has a good control effect and disturbance rejection ability. Meanwhile, the control method has less parameters to adjust and less calculation, which is very suitable for engineering applications.

Keywords: high aspect ratio; full-wing; lateral-directional control; without an aileron; differential thrust of propellers; nonlinear dynamic inversion; active disturbance rejection control; vector field path following; flight test

1. Introduction

High aspect ratio full-wings have a higher lift-drag ratio at low speed and simpler structure than the conventional configuration, so they are favorable for solar-powered UAVs. Meanwhile, the flat upper surface of high aspect ratio full-wings makes this configuration have a larger and more complete solar-cell laying area. The most famous high aspect ratio full-wing UAVs are Pathfinder and Helios [1], solar-powered UAVs designed by NASA. The high aspect ratio full-wing UAV researched in this paper consists of a central wing, two outer wings, and two vertical stabilizers, as is shown in Figure 1.

Limited by solar radiation energy, all solar-powered UAVs have high aspect ratio wings and ultra-low structures in order to improve aerodynamic efficiency and reduce structural weight. However, this makes wings prone to torsional deformation, and the aileron's control efficiency is very low, as well as aileron reversal may occur. Meanwhile, in order to reduce the weight, the high aspect ratio full-wing UAV usually does not have rudders. To solve the lateral-directional control problem,

high aspect ratio full-wing UAVs, such as Pathfinder [2], use the differential thrust of propellers instead of ailerons and rudders. Different from the aileron directly generating the rolling moment, the differential thrust of propellers will first produce sideslip and then rely on the lateral stability to produce the roll angle, so the stabilities of UAVs become essential.
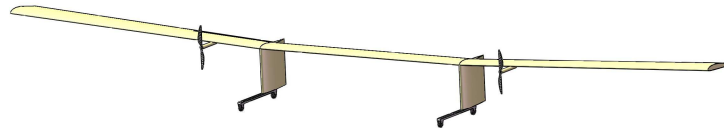

Figure 1. High aspect ratio full-wing configuration.

Due to the low flight speed and poor yaw static stability of the full-wing UAV, it is sensitive to wind field disturbances and speed changes during its flight. According to the cascade control theory, the lateral-directional control of full-wing UAVs can be divided into the lateral-directional attitude control and the lateral-directional trajectory control. For the former, Han [3] and Gao [4] proposed the theory of active disturbance rejection control, which is a control theory with a strong robust ability and easy engineering realization [5], and it is very suitable for flight control design [6–8]. Nonlinear dynamic inversion control (NDI) is widely used in flight control research [9–11]. The work in [12] showed that NDI has a good control effect, but it needs a precise mathematical model of the controlled drone. For the latter, the vector field trajectory tracking method, proposed by Nelson [13], is one of the most popular trajectory tracking methods presently [14–16]. Compared with other trajectory tracking methods, such as the line-of-sight method [17], the nonlinear guidance method [18], and the LQRmethod [19], Sujit's [20] research showed that the vector field method has the best wind resistance, which is a good choice to control high aspect ratio full-wing UAVs.

Based on the above analyses, this paper will focus on the lateral attitude control and trajectory control for a high aspect ratio full-wing UAV. First, a lateral-direction mathematical model of a full-wing configuration UAV with twin propellers is established, and its lateral-direction flying qualities are analyzed. Then, based on active disturbance rejection control (ADRC) and NDI theories, a full-wing UAV lateral attitude control law is designed, which uses the differential thrust of propellers as the control output. Third, the vector field trajectory tracking method is improved to meet the requirements of linear tracking control for this UAV. Finally, the control effects of the designed controller are verified with simulations and flight tests.

2. Mathematical Model and Flying Qualities

2.1. Lateral-Directional Mathematical Model

The lateral-directional mathematical model of a high aspect ratio full-wing UAV can be expressed as:

$$
\begin{cases}
\dot{v} = p\omega - ru + g\cos\theta\sin\phi + Y/M \\
\dot{\phi} = p + q\sin\phi\tan\theta + r\cos\phi\tan\theta \\
\dot{\psi} = q\sin\phi\sec\theta + r\cos\phi\sec\theta \\
\dot{p} = \Gamma_1 pq - \Gamma_2 qr + \Gamma_3 l + \Gamma_4 n \\
\dot{r} = \Gamma_5 pq - \Gamma_1 qr + \Gamma_4 l + \Gamma_6 n
\end{cases}
\tag{1}
$$

and:

$$
\begin{cases}
\Gamma = I_x I_z - I_{xz}^2, \Gamma_1 = I_{xz}\left(I_x - I_y + I_z\right)/\Gamma, \Gamma_2 = \left(I_z\left(I_z - I_y\right) + I_{xz}^2\right)/\Gamma \\
\Gamma_3 = I_z/\Gamma, \Gamma_4 = I_{xz}/\Gamma, \Gamma_5 = \left(I_x\left(I_x - I_y\right) + I_{xz}^2\right)/\Gamma, \Gamma_6 = I_x/\Gamma
\end{cases}
\tag{2}
$$

$$
Y = \bar{q}SC_{Y\beta}\beta
\tag{3}
$$

$$l = \bar{q}SbC_{l\beta}\beta + \frac{\bar{q}b^2}{2V_a}S\left(C_{lp}p + C_{lr}r\right) \tag{4}$$

$$n = \bar{q}SbC_{n\beta}\beta + \frac{\bar{q}b^2}{2V_a}S\left(C_{np}p + C_{nr}r\right) + \Delta F_p d_p \tag{5}$$

In the equations, I_x, I_y, I_z, and I_{xz} are the moments of inertia and the product of inertia, respectively. M is the mass. u, v, w are velocities in the body-fixed frame. p, q, r are angular rates in the body-fixed axes. β, θ, ϕ, and ψ are the sideslip angle, pitch angle, roll angle, and yaw angle. Y, l, n are the lateral force, roll, and yaw moments. $C_{Y\beta}, C_{l\beta}, C_{n\beta}$ are the lateral force derivative, roll, and yaw static stability derivative. C_{np}, C_{lr} are the dynamic cross derivatives, and C_{lp}, C_{nr} are the roll and yaw damping derivatives. Va, S, b are the airspeed, planform area, and wingspan of the aircraft. $\bar{q}$ is the dynamic pressure. ΔF_p is the differential thrust of propellers, while d_p is the distance between the propellers and the symmetric plane of the UAV.

The author of this paper improved the propeller thrust model proposed by Beard [21] through experimental data in the article [22].

$$F_p = \frac{1}{2}\rho S_p C_p\left(k_{p1}\delta_p{}^2 + k_{p2}\delta_p - V_p^2\right) \tag{6}$$

The testing picture of the propeller thrust and the propeller thrust fitting results is shown in Figures 2 and 3. The fitting R-squared reached 0.997.
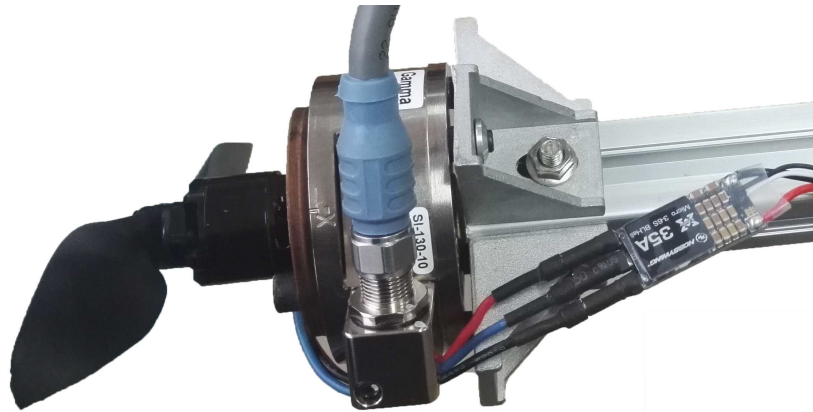

Figure 2. The testing picture of the propeller thrust.

Define $\Delta\delta_p$ as the differential throttle; the throttles of the left and right propellers are $\delta_{pl} = \delta_p + \Delta\delta_p$ and $\delta_{pr} = \delta_p - \Delta\delta_p$. Then, V_p of the left and right propellers are $V_{pl} = V_a + d_p r$ and $V_{pr} = V_a - d_p r$. The differential thrust of the propellers is:

$$\Delta F_p = F_{pl} - F_{pr} = \rho S_p C_p(2k_{p1}\delta_p\Delta\delta_p + k_{p2}\Delta\delta_p - 2V_a d_p r) \tag{7}$$

When the error between the course angle χ and the yaw angle ψ is not considered, the horizontal position of the drone can be expressed as:

$$\begin{cases} \dot{P}_x = V_e \sin\psi \\ \dot{P}_y = V_e \cos\psi \end{cases} \tag{8}$$

where V_e is the ground speed of the drone. P_x and P_y are the positions of the drone in the east and north directions.
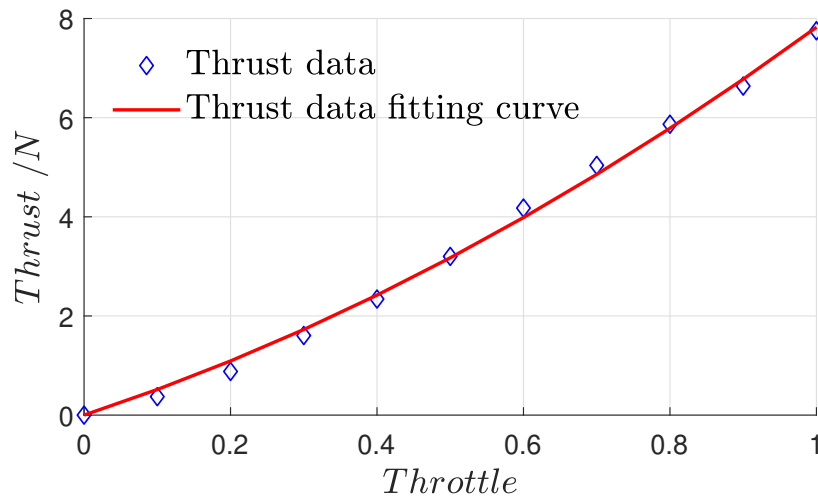
Figure 3. Propeller thrust fitting results.

2.2. Flying Qualities

The three-view and isometric drawings of the high aspect ratio full-wing configuration UAV in this paper are shown in Figure 4.
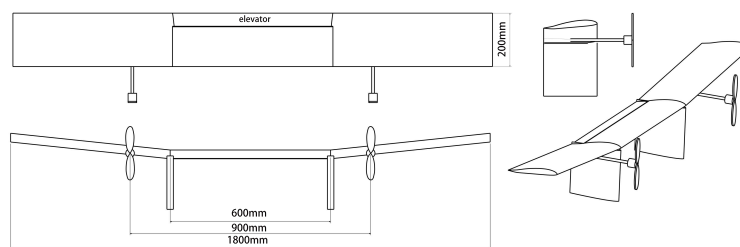

Figure 4. The three-view and isometric drawings of the high aspect ratio full-wing drone.

As shown in Figure 4, the UAV has a wingspan of 1.8 m and a chord length of 0.2 m. The wing is composed of three parts: the central wing and two outer wings. The larger dihedral angle of the outer wing reaches six degrees. Two vertical stabilizers are arranged below the central wing, and tires can be installed on the vertical stabilizers as the landing gears. Two motors are mounted on the outer wings, and the distance between them is 0.9 m.

In order to make a more intuitive comparison, the full-wing UAV in this paper is compared with a conventional configuration UAV with the same wingspan length, chord length, and a similar weight. Their basic parameters are shown in Table 1.

Table 1. The basic parameters of the full-wing and conventional configurations.

Basic Parameters	M	I_x	I_z	$C_{Y\beta}$	$C_{l\beta}$	$C_{n\beta}$	C_{lp}	C_{np}	C_{lr}	C_{nr}
full-wing configuration	1.053	0.160	0.164	−0.400	−0.118	0.020	−0.671	−0.040	0.113	−0.003
conventional configuration	1.090	0.111	0.208	−0.143	−0.143	0.016	−0.707	−0.036	0.102	−0.014

Table 1 shows that the full-wing drone weighs only 1.053 kg, and the wing load is 2.925 kg/m^2. I_x of the full-wing configuration is smaller than that of the conventional configuration, because the full-wing configuration has no fuselage; thus, it has a more reasonable inertial load distribution. Because of the tail, I_z of the conventional configuration is larger. The static stability derivatives $C_{l\beta}$ and $C_{n\beta}$ and the damping derivative C_{lp} are basically the same for both configurations. However, thanks to the larger vertical stabilizer, the side force derivative $C_{Y\beta}$ of the full-wing is three-times as large. Meanwhile, because of the tailless design, the yaw damping derivative C_{nr} of the full-wing is extremely small.

The lateral-directional modes of both configurations at $V_a = 11$ m/s are shown in Table 2.

Table 2. The lateral-directional modes of full-wing and conventional configurations.

Mode Parameters	Roll Subsidence Mode	Dutch Roll Mode			Spiral Mode
	Characteristic	Characteristic	Damping Ratio	Natural Frequency	Characteristic
full-wing	-13.34	$-0.26 \pm 1.48i$	0.17	1.50	-0.050
conventional	-18.98	$-0.55 \pm 3.39i$	0.16	3.44	-0.055

Table 2 shows that the roll subsidence mode and dutch roll mode characteristics of the conventional drone are 1.42- and 2.29-times as much as those of the full-wing drone. According to the MIL-F-8785C specification, even if the full-wing configuration does not have a tail, it can still satisfy the Class I flying quality of the lateral-directional mode. The analysis shows that $C_{Y\beta}$ may play an important role. Recalculate the lateral-directional modes of the full-wing drone in Table 3 after setting $C_{Y\beta}$ to -0.1, -0.2, -0.3, and -0.4 respectively.

Table 3. The lateral-directional modes of the full-wing drone at different $C_{Y\beta}$.

$C_{Y\beta}$	Roll Subsidence Mode	Dutch Roll Mode			Spiral Mode
	Characteristic	Characteristic	Damping Ratio	Natural Frequency	Characteristic
-0.1	-13.32	$0.020 \pm 1.48i$	-0.014	1.48	-0.050
-0.2	-13.33	$-0.088 \pm 1.49i$	0.059	1.49	-0.050
-0.3	-13.33	$-0.20 \pm 1.49i$	0.13	1.50	-0.051
-0.4	-13.34	$-0.26 \pm 1.48i$	0.17	1.50	-0.051

From Table 3, we can see that $C_{Y\beta}$ has little effect on the roll subsidence and spiral mode, but it has a very large impact on the real root and damping ratio of the dutch roll mode. Too small a $C_{Y\beta}$ will lead to the dutch roll mode of the full-wing drone being unstable. Since the vertical stabilizer is the most important component for generating lateral forces, it is important to select properly the size of the vertical stabilizers for the lateral-directional modes of the full-wing configuration.

3. Lateral-Directional Control Law Design

3.1. Lateral-Directional Attitude Control Law Based on ADRC and NDI

The lateral-directional attitude of UAVs can be divided into the roll angle and yaw angle. The full-wing drone in this paper has no aileron or rudder, so the yaw control moment can only be generated by the differential propeller thrust. Although the yaw control moment generated by the rudder in the paper [23] achieved roll angle control, the control process was not direct enough, and the response speed was slow. Therefore, this paper draws lessons from Pathfinder's [24] lateral-directional attitude control law, that is using the differential propeller thrust to control the yaw angle, while the roll angle is not considered in the control process.

When the roll angle and the roll angle rate are not taken into consideration, Equation (1) can be simplified as:

$$\begin{cases} \dot{\psi} = q \sin \phi \sec \theta + r \cos \phi \sec \theta \\ \dot{r} = \Gamma_5 pq - \Gamma_1 qr + \Gamma_4 l + \Gamma_6 n \end{cases} \tag{9}$$

Obviously, Equation (9) can be divided into a yaw angular rate loop and a yaw angle loop. According to the time scale separation theory, the yaw angle control loop and yaw rate control loop can be designed, respectively. Therefore, ADRC control with a strong disturbance rejection ability and good robustness was adopted in the yaw angle rate loop because it is sensitive to disturbance moment and has no accurate mathematical model, while the yaw angle loop does. Thus, using NDI

controller not only has a good control ability, but also solves the singularity problem that appears when $\psi = \pm 180°$ and the ADRC controller is used. The control structure is shown in Figure 5.
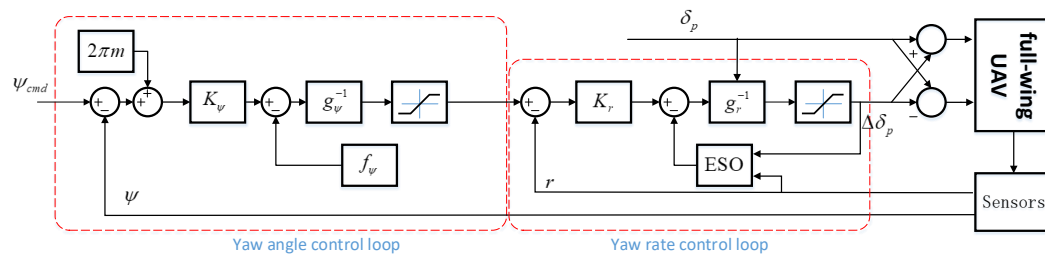

Figure 5. Structure diagram of lateral-directional attitude control law. ESO, extended state observer

3.1.1. Yaw Angle Control Loop

The first part of Equation (9) can be represented as:

$$\dot{\psi} = f_\psi + g_\psi r \tag{10}$$

where $f_\psi = q \sin \phi \sec \theta$ and $g_\psi = \cos \phi \sec \theta$.

Based on the NDI control theory, the feedback control law of the yaw angle is designed as follows:

$$\bar{r}_c = \left[K_\psi \left(\psi_c - \psi \right) - f_\psi \right] g_\psi^{-1} \tag{11}$$

Because there is a singularity in the yaw angle, Equation (11) can be improved as:

$$\bar{r}_c = \left[K_\psi \left(\psi_c - \psi + 2\pi n \right) - f_\psi \right] g_\psi^{-1} \tag{12}$$

where n is an integer that makes $-\pi < \psi_c - \psi + 2\pi n \leq \pi$. In order to prevent excessive yaw rate command, the command is limited to r_{cmax}.

$$r_c = \text{sat}(\bar{r}_c, -r_{cmax}, r_{cmax}) \tag{13}$$

where $\text{sat}(\cdot)$ is the saturation function.

3.1.2. Yaw Angle Rate Control Loop

The second part of Equation (9) can be expressed as:

$$\dot{r} = f_r + g_r \Delta \delta_p \tag{14}$$

g_r is the control efficiency of the differential propeller thrust:

$$g_r = \Gamma_6 \rho S_p C_p \left(2k_{p1} \delta_p + k_{p2} \right) \tag{15}$$

Obviously, the control efficiency of $\Delta \delta_p$ is related to throttle δ_p.

f_r is a multi-variable function of both the states and external disturbances, so f_r cannot be accurately measured and calculated in practice. In the ADRC control theory, f_r is called the total disturbance, which can be estimated by the extended state observer (ESO).

$$\begin{cases} e_r = \hat{r} - r \\ \dot{\hat{r}} = \hat{\Delta}_r - \beta_1 e_r + g_r \Delta \delta_p \\ \dot{\hat{\Delta}}_r = -\beta_2 \text{fal}(e, \sigma, \delta) \end{cases} \tag{16}$$

where $\hat{\Delta}_r$ is the observed value of f_r. β_1 and β_2 are the gains of ESO, whose larger parameters lead to a better performance, but easier divergence. $\mathrm{fal}(\cdot)$ is a nonlinear function defined as:

$$\mathrm{fal}(e, \sigma, \delta) = \begin{cases} \frac{e}{\delta^{1-\sigma}}, & |e| \leq \delta \\ |e|^{\sigma}\mathrm{sign}(e), & |e| > \delta \end{cases} \tag{17}$$

where $\mathrm{sign}(\cdot)$ is the signum function.

Based on the ADRC theory, the feedback control loop is designed as:

$$\Delta\bar{\delta}_p = \left(K_r(r_c - r) - \hat{\Delta}_r\right) g_r^{-1} \tag{18}$$

In practice, δ_{pl} and δ_{pr} must be in the range of $(0,1]$. It is necessary to limit $\Delta\delta_p$ in $\Delta\delta_{pmax}$ to prevent δ_{pl} and δ_{pr} from saturation.

$$\Delta\delta_p = \mathrm{sat}(\Delta\bar{\delta}_p, -\Delta\delta_{pmax}, \Delta\delta_{pmax}) \tag{19}$$

3.2. Lateral-Directional Trajectory Tracking Control Law Based on VF

Presently, the flight path of the UAV is still dominated by a linear trajectory, and a mission path is composed of many linear trajectories. The linear trajectory is usually defined by waypoints, and the line segment defined by two waypoints is a straight line trajectory, as shown in Figure 6.
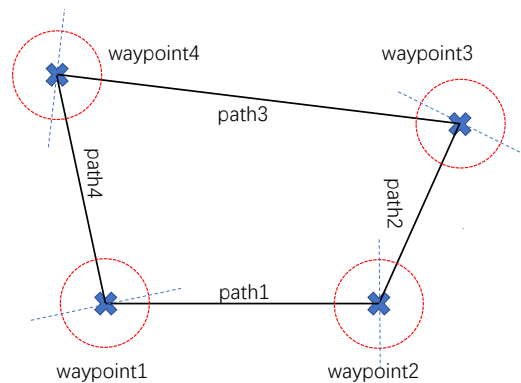

Figure 6. Waypoints and paths.

In practical applications, the drone cannot reach the waypoint accurately, so it is necessary to design the switching logic of the waypoints. One way is by judging the distance between the drone and its waypoint: assuming that the UAV is tracking path i, then when the distance between the drone and waypoint $i + 1$ is less than R, the tracking path is switched to $i + 1$. However, the flying speed of the high aspect ratio full-wing UAV in this paper is too low, and it may not be able to reach the waypoint in a strong wind. Therefore, it is necessary to supplement the switching logic. Another way is by judging the relative position of the drone and its path: assuming that the UAV is tracking path i, the dotted line in Figure 6 passes through the waypoint $i + 1$ and is perpendicular to path i. When the drone passes through this dotted line, the tracking path is switched to $i + 1$.

Figure 7 shows the calculation process of the waypoint switching logic. First, C_{wp} and L_{wp} are the current and last target waypoints, so the line between the two waypoints is the current path. wp_n is the number of waypoints. $C_{wp} < 1$ or $C_{wp} > wp_n$ are irrational; when this happens, set $C_{wp} = 1$. When $C_{wp} = 1$, set $L_{wp} = wp_n$; thus, let the waypoints form a closed loop. Second, determine whether the waypoint needs to be switched considering the distance between the drone and the waypoint or the relative position of the path. If necessary, add one to the current waypoint, which is $C_{wp}+ = 1$. $C_{wpx}, C_{wpy}, L_{wpx}$ and L_{wpy} are the east and north positions of the current and last target waypoints.

P_x and P_y are the drone's positions. Finally, calculate the direction angle of the straight line path ψ_t and the distance between the drone and path d.
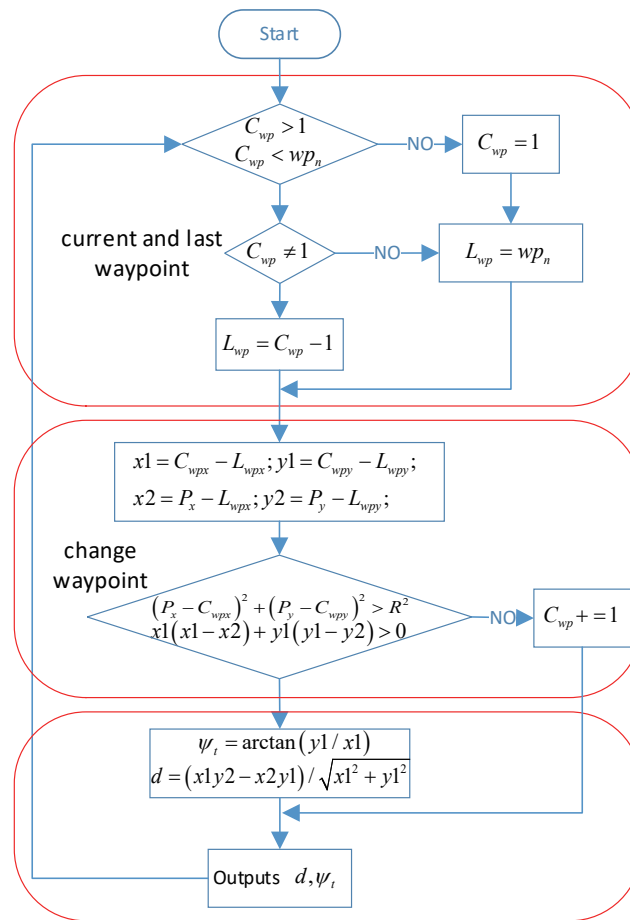

Figure 7. Switching logic of the waypoints.

Presently, most small UAVs use the global navigation satellite system (GNSS) to get 3D position information in the World Geodetic System 1984 (WGS84) coordinate system. WGS84 is too complex for small UAVs. In order to simplify the calculation, the Earth is approximated as a sphere. After ignoring the flying height, the relative distance between the two points can be expressed as:

$$\begin{cases} x = R_e \cos{(lat2)}(lat2 - lat1) \\ y = R_e(lon2 - lon1) \end{cases} \tag{20}$$

where x, y are the distances between the two points in the east and north. $R_e = 6371$ km is the average radius of the Earth. $lat1, lon1, lat2,$ and $lon2$ are the latitudes and longitudes of the two points. During the experiment, all the positions are obtained by calculating the relative positions in relation to Waypoint 1.

When analyzing a straight path separately, the position relationship between the drone and the path is as shown in Figure 8.
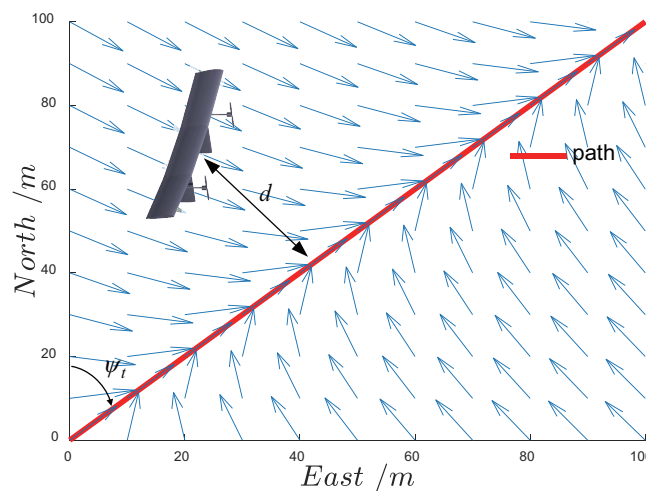
Figure 8. Schematic diagram of the lateral-directional trajectory tracking control law.

d is the distance between the drone and the path. ψ_t is the direction angle of the straight line path. When the error between the course angle χ and the yaw angle ψ is not considered:

$$d = V_e \sin (\psi - \psi_t) \tag{21}$$

Based on the vector field (VF) trajectory tracking theory, the yaw angle control command can be expressed as:

$$\psi_c = \psi_t - \psi^\infty \frac{2}{\pi} \tan^{-1}(K_d d) + 2\pi m \tag{22}$$

When d is large enough, the UAV is directed to approach the path at a ψ^∞ angle, so the range of ψ^∞ is $\left(0, \frac{\pi}{2}\right]$. m is an integer that ensures $-\pi < \psi_c \leq \pi$.

Obviously, Formula (22) does not consider the effect of the velocity. Usually, the higher the speed, the smaller K_d should be. Therefore, the parameter K_d is redefined as:

$$K_d = \bar{K}_d / \text{sat} \left(V_e, V_{min}, inf\right) \tag{23}$$

4. Simulations and Flight Tests

Verify the designed lateral-directional control law through simulations and flight tests. The control law's parameters are shown in Table 4.

Table 4. The lateral-directional control law parameters.

Parameters	K_ψ	r_{cmax}	β_1	β_2	σ	δ	K_r	$\Delta\delta_{pmax}$	ψ^∞	$\bar{K}_d$
Values	1	$\frac{\pi}{9}$	300	400	0.5	0.1	10	0.2	$\frac{\pi}{4}$	0.75
Equation	(11)	(13)	(16)	(16)	(17)	(17)	(18)	(19)	(22)	(23)

4.1. Simulations

4.1.1. Attitude Control

Verify the effectiveness, robustness, and anti-disturbance ability of the proposed yaw angle control law based on the nonlinear dynamic inversion and active disturbance rejection control (NDI-ADRC) theory with simulations. Figure 9 is the response curves of the NDI-ADRC yaw angle controller when tracking commands at 8, 11, and 17 m/s. In order to verify the robustness of the controller, the aerodynamic parameters is 30% bigger than the original ones, while the control efficiency of the differential propeller thrust is 20% smaller during the simulations. At the same time, in order to test

the wind resistance ability of the controller, when $t = 100$ s, add a cross discrete gust wind in the simulations. The gust amplitude and length are 3 m/s and 50 m. Figure 10 is the response curves of the NDI-ADRC controller when tracking the command under the condition of an 11-m/s speed and disturbed by yaw moment $n = 1.2 \, \text{sign} \left(\sin \left(\frac{\pi}{4} t \right) \right) N \cdot m$. Comparing the control effects, the PID controller has the same gain parameters as the NDI-ADRC controller.

Figure 9a shows that even if the aerodynamic parameters and the control efficiency of the differential propeller thrust are changed, the NDI-ADRC yaw angler controller can still track command signals effectively at different flying speeds. The tracking process is smooth and without overshoot. The rise time is about 5 s when tracking a 90° step signal in the time range of 45–50 s. Figure 9b shows the sideslip angle $\beta < \pm 8°$ during the simulation. As shown in Figure 9c, the output time of the differential propeller thrust is very shot, and there is no output in most cases. From Figure 9a,b, we can learn that the gust will influence the sideslip angle β. According to Table 1, we can see $\left| C_{l\beta} \right| \gg \left| C_{n\beta} \right|$, so the cross gust wind mainly affects the roll angle, not the yaw angle.

As shown in Figure 10a, the average tracking error and error amplitude of the NDI-ADRC controller are 0.37° and 1.00° during 10–40 s, while those of PID controller are 2.30° and 2.92°. Obviously, the NDI-ADRC controller has a much better anti-disturbance ability than the PID controller, which is mainly because ESO has a very effective observation of the disturbance in Figure 10d. Although the disturbance moment of 1.2 N is very large for such a small aircraft, the differential propeller thrust is still not saturated, which shows that the control efficiency of the differential propeller thrust is very high in flight.
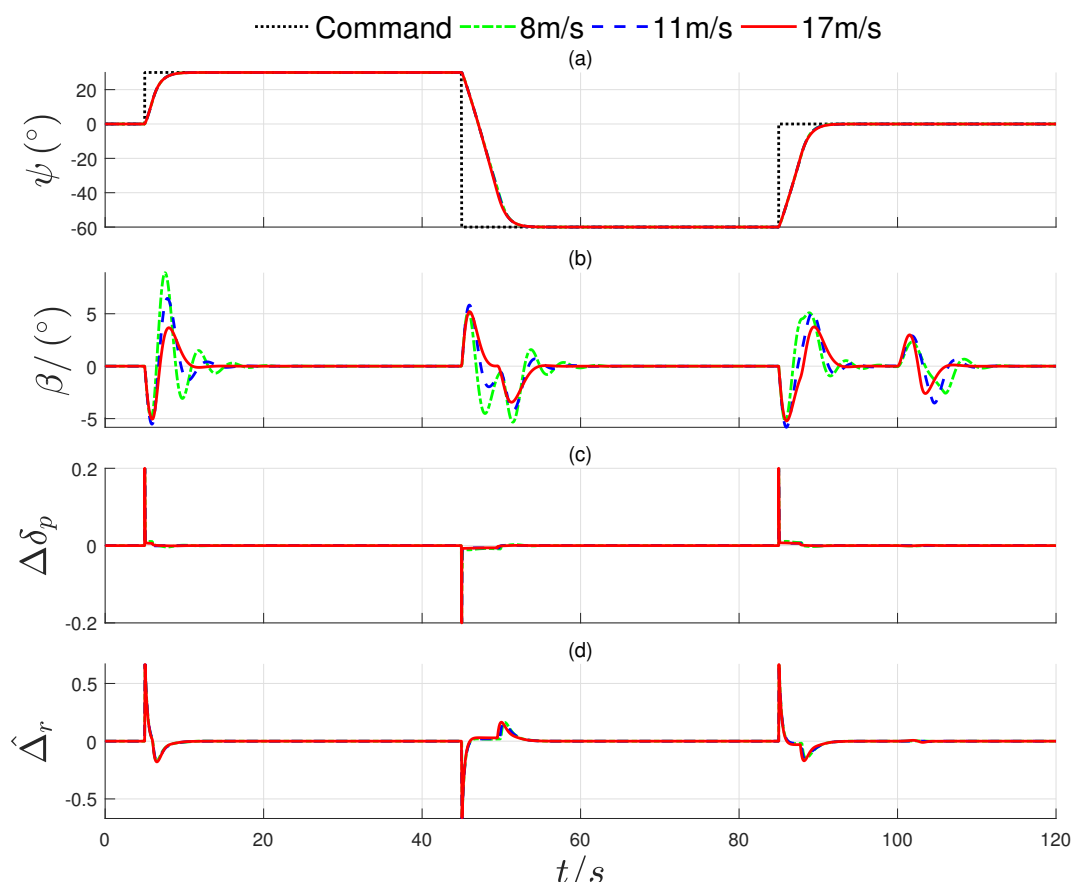

Figure 9. The yaw angle (**a**), side-slip angle (**b**), differential propeller thrust (**c**) and observer (**d**) curves of the nonlinear dynamic inversion and active disturbance rejection control (NDI-ADRC) yaw angle controller when tracking the command at different speeds.
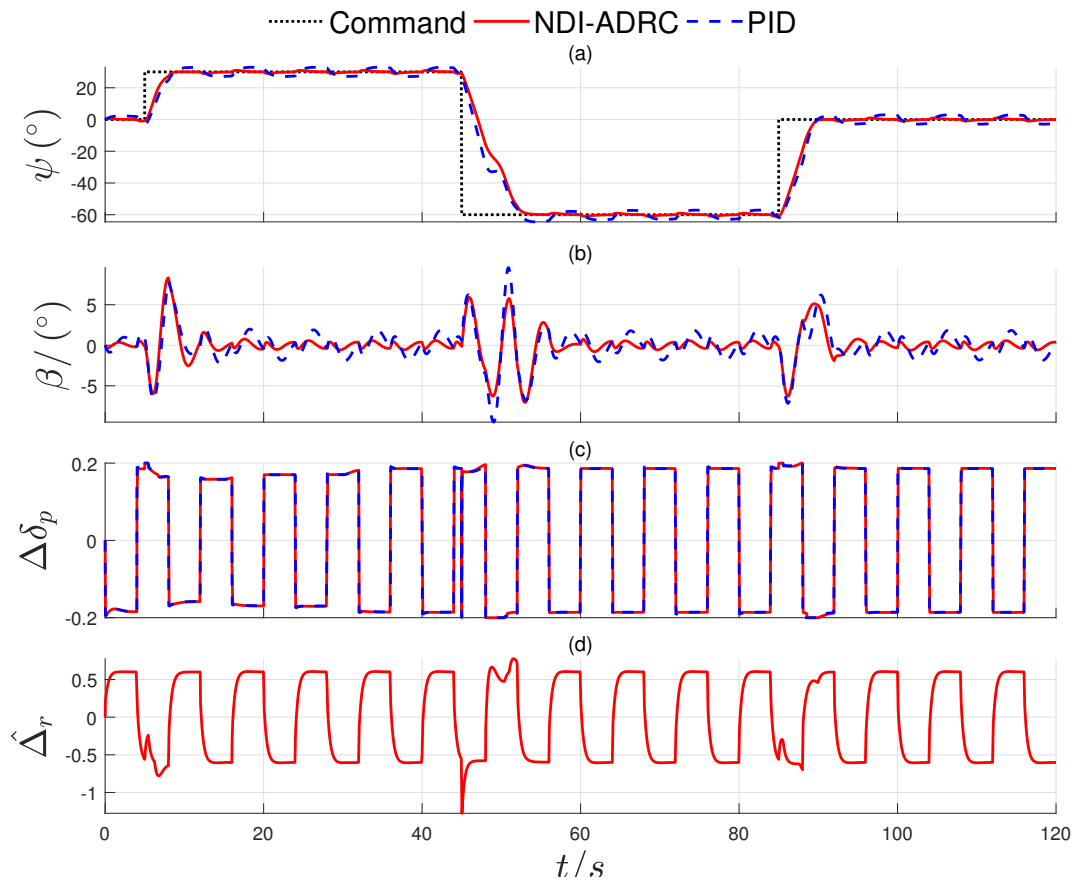
Figure 10. The yaw angle (**a**), side-slip angle (**b**), differential propeller thrust (**c**) and observer (**d**) curves of NDI-ADRC and PID controllers for the disturbed yaw moment.

4.1.2. Trajectory Tracking Control

Verify the effectiveness of the trajectory tracking control law based on VF theory. Figure 11 shows the flight path when the full-wing drone is tracking a four-sided path square with a side length of 300 m. Arrows are the drone's heading angles at each position. Based on the simulation of Figure 11, Figure 12 is the experimental results after adding a 3-m/s constant east wind at the beginning of the simulation.

As shown in Figure 11, the improved VF method can control the drone to track the linear trajectory at different speeds. Meanwhile, by adjusting parameter *R*, the waypoint switching process is smooth and without overshoot. Figure 12 shows that wind will reduce the accuracy of UAV trajectory tracking. When the flight is relatively stable, both Paths 1 and 3 have errors of about 10 m. Observing the trajectory curve of the tracking Path 3, we find a lower the speed, the more it is influenced by wind. Compared with Path 3, Path 1 is less affected by wind. This is because the UAV will roll to the right when it switches from Path 2 to Path 3, and the wind field will intensify the roll. However, when it switches from Path 4 to Path 1, the roll-induced sideslip is opposite the wind-induced sideslip, which forms a counteraction effect.
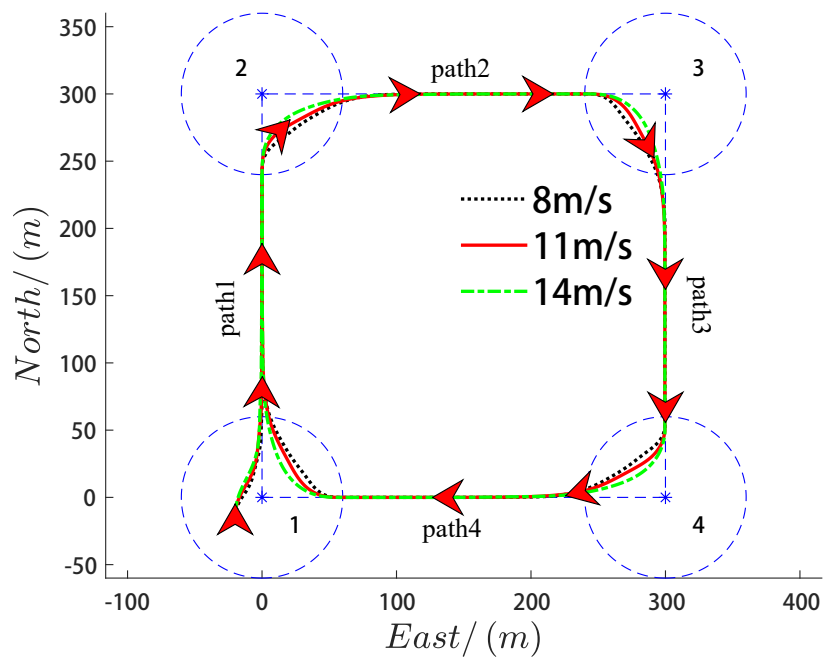
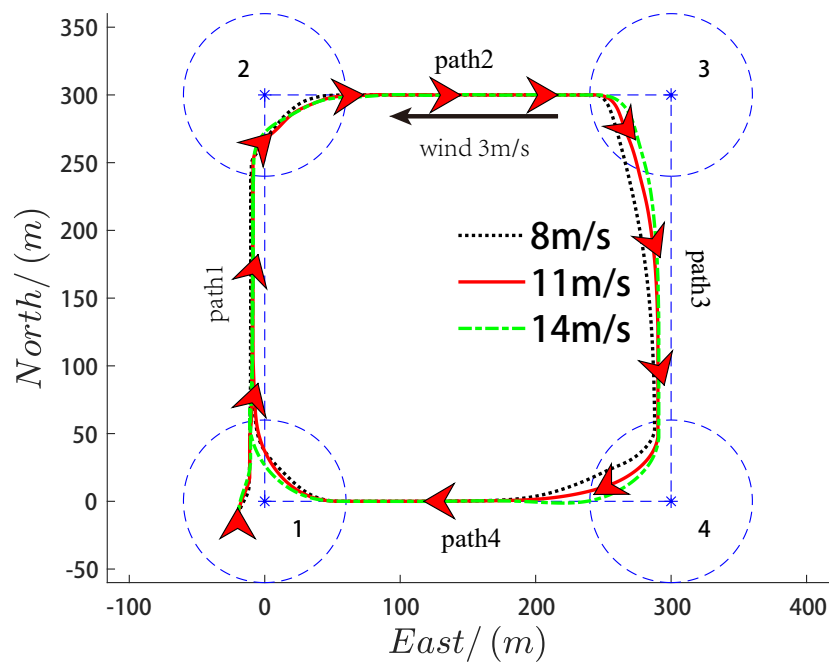**Figure 11.** The flight path of the full-wing drone when tracking a four-sided path.

Figure 12. The flight path of the full-wing drone when tracking a four-sided path in the east wind.

4.2. Flight Tests

The flight test of the lateral-directional control method for the high aspect ratio full-wing UAV designed in this paper was carried out through experiments.

4.2.1. Flight Test Bed

In order to solve the problems of a long flight test cycle and high cost, an experimental test bed of the UAV with a large aspect ratio and full-wing configuration was designed, which consisted of a small aircraft, a small autopilot, and some accessories.

The small aircraft is shown in Figure 13, the shape of which is exactly the same as in Figure 4. Pictures of the flight process are shown in Figure 14, and a flight video can be found at https://www.bilibili.com/video/av48090653.

Figure 13. The high aspect ratio full-wing UAV for the flight experiments.

Figure 14. The high aspect ratio full-wing UAV in flight.

Figure 15 shows the connection of the small autopilot and its electronic equipment. The control law code of the small autopilot system adopted graphical programming and automatic code generation technology, which greatly shortened the period of modifying the control law and accelerated the experimental cycle. The sensors of the autopilot and accessories are shown in Table 5.
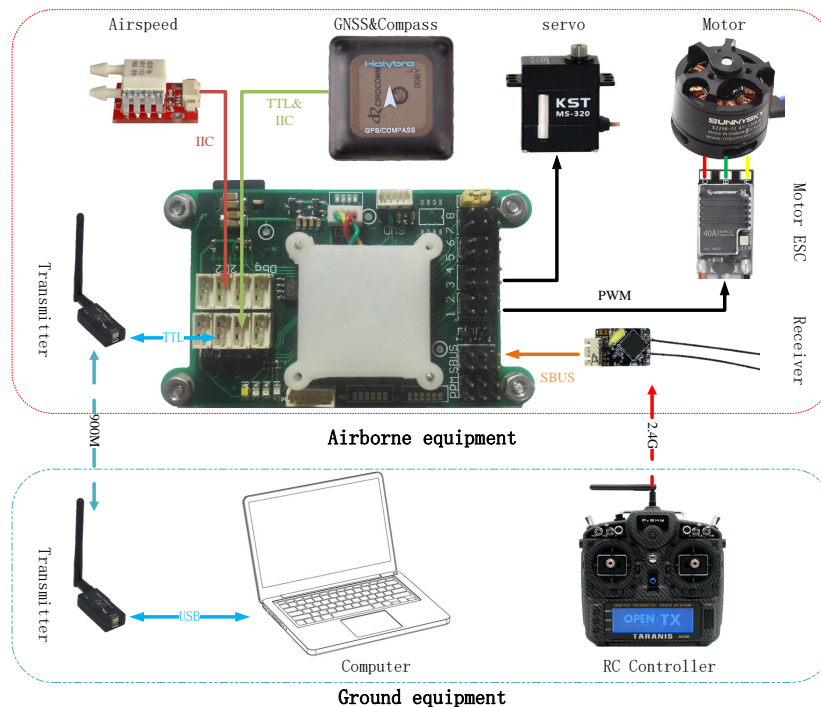

Figure 15. The connection of the small autopilot and its electronic equipment.

Table 5. Sensors of the autopilot and accessory.

Processor	Accelerate & Gyro	Compass	Air Speed	GNSS	Motor	Propeller
Stm32f407	Mpu6050	Hmc5983	Ms4525do	Ublox m8n	2212-1400	APC8060

4.2.2. Flight Test Results

Figure 16 shows the trajectory curve of the UAV with full-wing configuration tracking four-sided paths during the experiment. Figure 17 shows the response curves of yaw angle, yaw angular rate, differential propeller thrust and ESO during the flight.
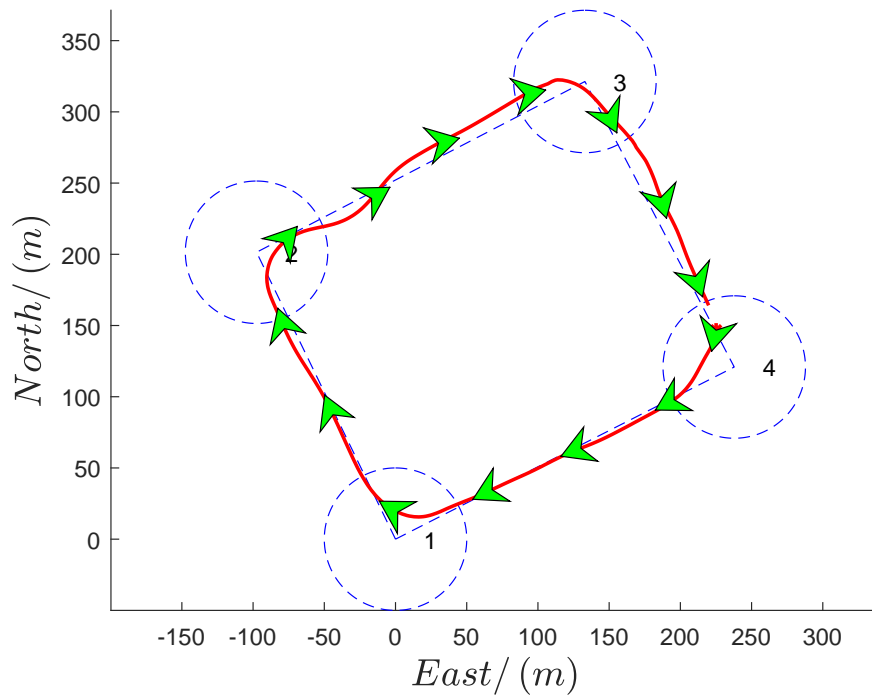
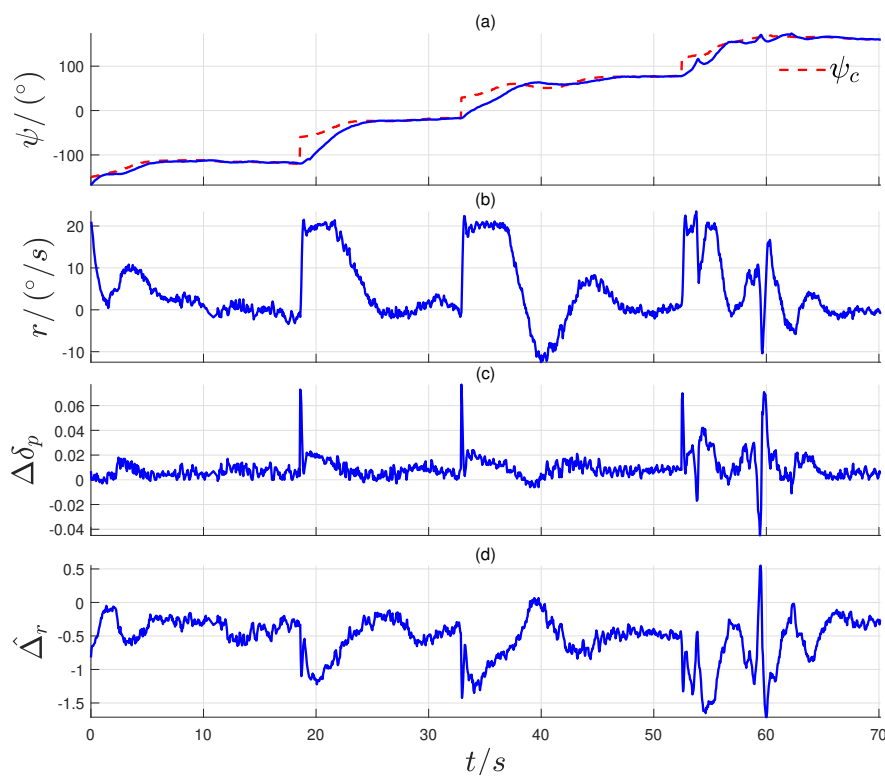**Figure 16.** The trajectory curve of the drone when tracking four-sided paths.

Figure 17. The yaw angle (**a**), yaw angular rate (**b**), differential propeller thrust (**c**) and observer (**d**) curves during the flight.

Figure 16 shows that the improved vector field trajectory tracking method still had a good control effect in the flight experiments. The maximum error of the controller was 12 m, and the average error was 5.06 m, which can meet the requirements of practical applications.

The curve of 18–30 s in Figure 17a shows that the response time of the NDI-ADRC yaw angle controller was about 5 s, which was the same as in the simulations. When the command signal was stable at 10–18 s, the average tracking error was 0.91°. Therefore, the NDI-ADRC yaw angle controller also had good control effects and control accuracy in the experiments. The curves of 18–25 s and 33–38 s in Figure 17b show that the yaw angular rate reached the maximum designed value 20°/s, but the overshoot was only 2°/s. Figure 17c shows that the output of the differential propeller thrust was very small, which corresponds to the simulation results. Therefore, the energy consumption of the differential propeller thrust was very small, which is suitable for the solar UAV with strict energy consumption requirements.

5. Conclusions

This paper presents a lateral-directional control method for the high aspect ratio full-wing UAV without an aileron and rudder by using the differential thrust of propellers as the output. By doing research on flight stability, the yaw angle attitude control and trajectory tracking of the full-wing UAV through simulations and flight tests, the authors demonstrated the following key points:

(a) $C_{Y\beta}$ was very important for the dutch roll mode of the high aspect ratio full-wing UAV. Large $C_{Y\beta}$ can significantly improve the dutch roll mode damping.

(b) It was feasible and effective to use the yaw angle instead of the roll angle as the controlled state for the high aspect ratio full-wing UAV. The differential propeller thrust had good control efficiency, which can replace an aileron and rudder to control the drone's lateral-direction.

(c) The simulation and experiment results show that the lateral-directional control method for the high aspect ratio full-wing UAV designed in this paper had a good control effect, robustness, and disturbance rejection ability. At the same time, the controller had less calculation, fewer parameters to be adjusted, and a simple implementation process, which is very important for engineering applications.

Author Contributions: Conceptualization, X.Z. (Xiaoping Zhu). and Z.Z.; methodology, Z.M.; software, Z.M.; writing, original draft preparation, Z.M.; writing, review and editing, Z.M.; project administration, X.Z. (Xu Zou).; data curation, X.Z. (Xin Zhao).

References

1. Ehernberger, L.J.; Donohue, C.; Teets, E.H. A review of solar-powered aircraft flight activity at the Pacific missile range test facility, Kauai, Hawaii. In Proceedings of the 11th AMS Conference on Aviation, Range, and Aerospace Meteorology, Hyannis, MA, USA, 4–8 October 2004; pp. 1–6.

2. Colella, N.J.; Wenneker, G.S. Pathfinder. Developing a solar rechargeable aircraft. *IEEE Potentials* **1996**, *15*, 18–23. [CrossRef]

3. Han, J. From PID to Active Disturbance Rejection Control. *IEEE Trans. Ind. Electron.* **2009**, *56*, 900–906. [CrossRef]

4. Gao, Z. Active disturbance rejection control: A paradigm shift in feedback control system design. In Proceedings of the IEEE American Control Conference, Minneapolis, MN, USA, 14–16 June 2006; pp. 2399–2405.

5. Li, H.; He, B.; Yin, Q.; Mu, X.; Zhang, J.; Wan, J.; Wang, D.; Shen, Y. Fuzzy Optimized MFAC Based on ADRC in AUV Heading Control. *Electronics* **2019**, *8*, 608. [CrossRef]

6. Lotufo, M.A.; Colangelo, L.; Perez-Montenegro, C.; Canuto, E.; Novara, C. UAV quadrotor attitude control: An ADRC-EMC combined approach. *Control Eng. Pract.* **2019**, *84*, 13–22. [CrossRef]

7. Sun, J.; Pu, Z.; Yi, J. Conditional disturbance negation based active disturbance rejection control for hypersonic vehicles. *Control Eng. Pract.* **2019**, *84*, 159–171. [CrossRef]

8. Zhang, Y.; Chen, Z.; Zhang, X.; Sun, Q.; Sun, M. A novel control scheme for quadrotor UAV based upon active disturbance rejection control. *Aerosp. Sci. Technol.* **2018**, *79*, 601–609. [CrossRef]

9. Fields, M.A. Flight controller learning based on real-time model estimation of a quadrotor aircraft. *Proc. Inst. Mech. Eng. Part G J. Aerosp. Eng.* **2019**, *233*, 3298–3312. [CrossRef]

10. Wang, X.; Van Kampen, E.; Chu, Q.P.; De Breuker, R. Flexible Aircraft Gust Load Alleviation with Incremental Nonlinear Dynamic Inversion. *J. Guid. Control Dyn.* **2019**, *42*, 1519–1536. [CrossRef]

11. Tripathi, A.K.; Patel, V.V.; Padhi, R. Autonomous Landing of UAVs under Unknown Disturbances using NDI Autopilot with L-1 Adaptive Augmentation. *IFAC PapersOnline* **2017**, *50*, 3680–3684. [CrossRef]

12. Snell, S.A.; Nns, D.F.; Arrard, W.L. Nonlinear inversion flight control for a supermaneuverable aircraft. *J. Guid. Control Dyn.* **1992**, *15*, 976–984. [CrossRef]

13. Nelson, D.R.; Barber, D.B.; McLain, T.W.; Beard, R.W. Vector field path following for miniature air vehicles. *IEEE Trans. Robot.* **2007**, *23*, 519–529. [CrossRef]

14. Oh, H.; Kim, S. Persistent standoff tracking guidance using constrained particle filter for multiple UAVs. *Aerosp. Sci. Technol.* **2019**, *84*, 257–264. [CrossRef]

15. Yu, Z.; Qu, Y.; Zhang, Y. Safe Control of Trailing UAV in Close Formation Flight against Actuator Fault and Wake Vortex Effect. *Aerosp. Sci. Technol.* **2018**, *77*, 189–205. [CrossRef]

16. Kownacki, C.; Ambroziak, L. Local and Asymmetrical Potential Field Approach to Leader Tracking Problem in Rigid Formations of Fixed-Wing UAVs. *Aerosp. Sci. Technol.* **2017**, *68*, 465–474. [CrossRef]

17. Fossen, T.I.; Pettersen, K.Y.; Galeazzi, R. Line-of-Sight Path Following for Dubins Paths With Adaptive Sideslip Compensation of Drift Forces. *IEEE Trans. Control Syst. Technol.* **2015**, *23*, 820–827. [CrossRef]

18. Park, S.; Deyst, J.; How, J.P. Performance and Lyapunov Stability of a Nonlinear Path Following Guidance Method. *J. Guid. Control Dyn.* **2007**, *30*, 1718–1728. [CrossRef]

19. Lee, S.; Cho, A.; Kee, C. Integrated waypoint path generation and following of an unmanned aerial vehicle. *Aircr. Eng. Aerosp. Technol.* **2010**, *82*, 296–304. [CrossRef]

20. Sujit, P.; Saripalli, S.; Sousa, J.B. Unmanned aerial vehicle path following: A survey and analysis of algorithms for fixed-wing unmanned aerial vehicless. *IEEE Control Syst.* **2014**, *34*, 42–59.

21. Beard, R.W.; McLain, T.W. *Small Unmanned Aircraft: Theory and Practice*; Princeton University Press: Princeton, NJ, USA, 2012.

22. Ma, Z.; Zhu, X.; Zhou, Z. On-ground lateral direction control for an unswept flying-wing UAV. *Aeronaut. J.* **2019**, *123*, 416–432. [CrossRef]

23. Meola, D.; Iannelli, L.; Glielmo, L. Flight control system for small-size unmanned aerial vehicles: Design and software-in-the-loop validation. In Proceedings of the Mediterranean Conference on Control & Automation, Chania, Greece, 25–28 June 2013; IEEE: Platanias, Greece, 2013; pp. 357–362.

24. Herwitz, S.; Dunagan, S.; Sullivan, D.; Higgins, R.; Johnson, L.; Zheng, J.; Slye, R.; Brass, J.; Leung, J.; Gallmeyer, B.; et al. Solar-powered UAV Mission for Agricultural Decision Support. In Proceedings of the 2003 IEEE International Geoscience and Remote Sensing Symposium, Toulouse, France, 21–25 July 2003; Volume 3, pp. 1692–1694. [CrossRef]